ALTAR/TABLE: A PLATFORM FOR PLAUSIBLE AUDITORY AUGMENTATION

Marian Weger[1], *Thomas Hermann*[2], *Robert Höldrich*[1]

[1] IEM, University of Music and Performing Arts, Graz, Austria
[2] Ambient Intelligence Group, CITEC, Bielefeld University, Bielefeld, Germany
weger@iem.at, thermann@techfak.uni-bielefeld.de, hoeldrich@iem.at

ABSTRACT

Auditory feedback from everyday interactions can be augmented to project digital information in the physical world. For that purpose, auditory augmentation modulates irrelevant aspects of already existing sounds while at the same time preserving relevant ones. A strategy for maintaining a certain level of plausibility is to metaphorically modulate the physical object itself. By mapping information to physical parameters instead of arbitrary sound parameters, it is assumed that even untrained users can draw on prior knowledge. Here we present AltAR/table, a hard- and software platform for plausible auditory augmentation of flat surfaces. It renders accurate augmentations of rectangular plates by capturing the structure-borne sound, feeding it through a physical sound model, and playing it back through the same object in real time. The implementation solves basic problems of equalization, active feedback control, spatialization, hand tracking, and low-latency signal processing. AltAR/table provides the technical foundations of object-centered auditory augmentations, for embedding sonifications into everyday objects such as tables, walls, or floors.

1. INTRODUCTION

An important kind of auditory feedback is the sound we perceive in reaction to our physical interactions: it conveys information about the ongoing physical processes — information that lets us stay within the sonic interaction loop and adapt our operations to the given conditions without requiring much conscious effort. More generally, the interaction loop integrating sound and other sensory modalities permits the tools we use to mediate our actions to effectively become an extension of our body. With growing complexity of the tools, e.g., from basic hand tools via mechanic machines to digital devices, the amount of useful information in the original auditory feedback decreases. This lack of usable auditory feedback in modern appliances highlights the need for sonic interaction design in general and auditory augmentation in particular. In auditory augmentation [1], [2], the original auditory feedback is modulated by external data in order to become augmented auditory feedback which thus comprises a sonification.

We assume that to be accepted by users, augmented auditory feedback needs to be *plausible* and usable with respect to the given physical interaction and with respect to information from other sensory modalities [3]. These requirements limit the parameter space for auditory augmentation and thus limit the total information capacity of the associated communication channel (see [3] for further information on the concept of plausible auditory augmentation). Especially interactions with the digital environment benefit from reality-based interactions that make digital information tangible and thus allow users to behave naturally by projecting their knowledge from the physical environment [4]–[6]. Auditory augmentation builds on top of established concepts such as *blended sonification* [7] and *model-based sonification* [8].

Back in 2010, Stockman [9] had raised the infamous question: "what can we take into the research arena of auditory displays from our every day experiences of listening?" Since then, various everyday objects have been augmented: computer keyboards [1], rooms [10], [11], doors [12], production systems [13], cars [14], showers [15], coat racks [16], flotsam [17], and stethoscopes [18].

We present AltAR/table[1], an augmented table which captures the original auditory feedback, feeds it through the physical model of a rectangular plate, and projects the result in real time (see Fig. 1). External data is sonified in a plausible way by mapping it to physical parameters of the model plate. To avoid visible loudspeakers as far as possible, we use structure-borne exciters which transform the interface plate into a bending wave loudspeaker. The hardware platform is designed to be put on top of a normal table, to work somehow similar to a touchscreen — with an auditory instead of a visual display. Its main purpose is to host the physical sound model of a rectangular plate, i.e., to capture the original auditory feedback, feed it through the model plate, and project the augmented auditory feedback into the physical environment of the user. Practical applications in the form of sonifications based on previous development stages comprise the *Mondrian table* and the

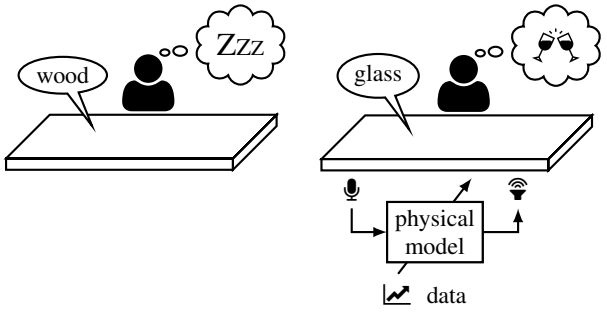

(a) Normal table. (b) Augmented table.

Figure 1: The concept of AltAR/table. A demonstration video is provided here: https://phaidra.kug.ac.at/o:126460

[1] AltAR stands for alternative auditory reality

https://doi.org/10.21785/icad2022.005

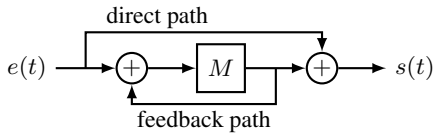

Figure 2: Simplified block diagram of an auditory augmentation system with input $e(t)$, transfer function M, and output $s(t)$.

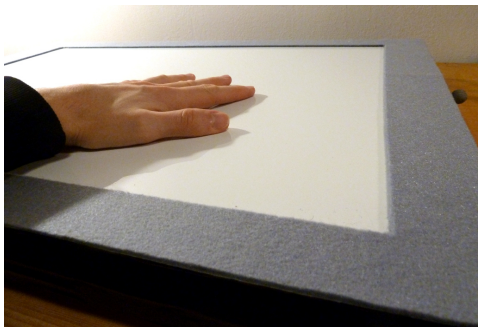

Figure 3: The AltAR/table hardware platform (top).

auditory coloring book [3], as well as prototypes for augmented writing, exploratory data analysis, and assisted object positioning [2].

The rest of this article is structured as follows. We start with the hardware apparatus in Sec. 2 and the physical sound synthesis model in Sec. 3. Technical challenges such as position tracking, output calibration, as well as noise and feedback control are outlined in Sec. 4.1, 4.2, and 4.3, respectively. We draw some final conclusions in Sec. 5.

2. HARDWARE PLATFORM

If assuming a single input and output channel, basic auditory augmentation systems follow the block diagram in Fig. 2. The excitation signal $e(t)$ that is generated by the user's action is filtered by the transfer function M of the system. What reaches the ears is the output signal $s(t)$. In addition to the main signal path, there are two additional paths that are generally undesirable: the original auditory feedback that reaches the ears via the direct path, and the acoustic feedback between loudspeaker and microphone which can lead to instability and thus howling.

A photo of the AltAR/table is shown in Fig. 3. The interface is based around a $0.7\,\mathrm{m} \times 0.5\,\mathrm{m}$ Dibond aluminum-polyethylene composite plate of thickness $3\,\mathrm{mm}$. It represents a compromise between several conflicting interests: strongly damped (minimal original auditory feedback), good sound conduction (for capturing excitation by contact microphones), and thin and elastic (for acting as bending wave loudspeaker). The interface plate sits on a particle board frame which stands on rubber feet (see Fig. 4). Overlapping regions are covered with felt on top and bottom to provide damping while the inner region of $594\,\mathrm{mm} \times 420\,\mathrm{mm}$ (DIN A2) can freely vibrate.

On the bottom side, 5 structure-borne exciters (Visaton EX 30 S, $8\,\Omega$) and 6 piezo-electric contact microphones (3 cm piezo disks) are mounted to the interface plate by using 3M VHB double-sided adhesive tape. Four of the piezos are placed near the corners ($5\,\mathrm{mm}$ distance to the frame), two others are placed in the center so that their distance between each other ($24\,\mathrm{cm}$) equals their distance to the nearby corner-piezos, respectively. The exciters are placed halfway between neighboring piezos, ensuring a symmetric arrangement with maximum distance between exciters and piezos.

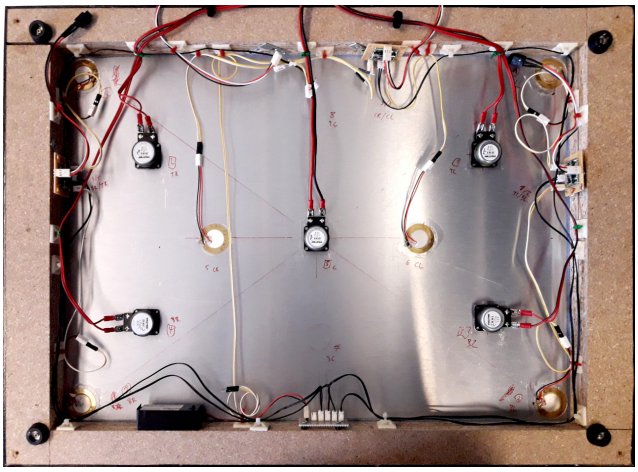

Figure 4: The AltAR/table hardware platform (bottom).

The piezo disks require a buffer preamp for impedance matching (see block diagram in Fig. 5). We employ 3 Schatten Design MicroPre 2-channel buffers, powered by a $9\,\mathrm{V}$ battery or Boss PSA-230P power supply. Their outputs are fed into three Samson S-direct Plus 2-channel DI boxes due to the longer cable run to the Behringer ADA8000 AD/DA converter. Two calibration microphones are connected directly to the ADA8000. The exciters are driven by a Hypex UcD36MP V3 6-channel power amplifier. Two Genelec 8020CPM loudspeakers which are mounted on the table serve as low-frequency extension. Audio processing is done on a PC running Debian GNU/Linux, through an RME HDSPe MADI FX soundcard and ADI-648 ADAT-to-MADI converter. Both data and audio signal processing are mainly implemented in the SuperCollider 3 language[2].

Each input channel (piezo) is processed separately and then spatialized to the output channels (exciters). This is done via distance-based amplitude panning (DBAP), following its original definition by [19]. For AltAR/table, we use a $6\,\mathrm{dB}$ roll-off, and an effectively negligible $1\,\mathrm{mm}$ source size.

As the exciters are not able to radiate sufficient power at frequencies below $200\,\mathrm{Hz}$, their frequency range is extended down to $70\,\mathrm{Hz}$ by two loudspeakers. Frequency crossover is set to $250\,\mathrm{Hz}$. The exciter channels are distributed to the loudspeakers by a simple cosine panning law which preserves constant power.

3. PHYSICAL MODEL OF A RECTANGULAR PLATE

3.1. The impulse response of a rectangular plate

According to [20], the impulse response of a rectangular plate at position (x, y), subjected to a point force at excitation position (x_0, y_0), is

[2]SuperCollider: `https://supercollider.github.io/`

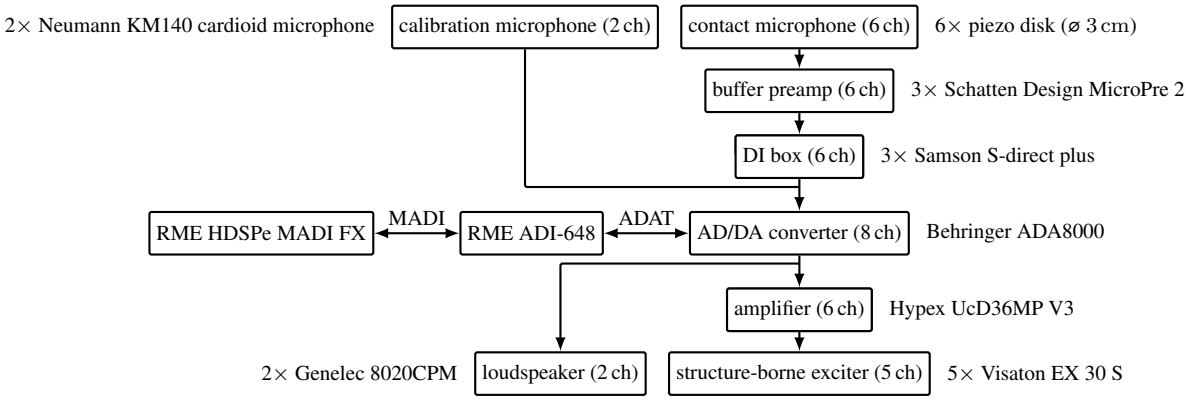

Figure 5: Block diagram of the hardware signal flow of the AltAR/table platform.

$$w(x,y,t) = \sum_{n=0}^{N}\sum_{m=0}^{M} \underbrace{\frac{\Theta_{mn}(x,y)\Theta_{mn}(x_0,y_0)}{\omega_{\mathrm{r},mn} M_{mn}}}_{\text{amplitude } A_{mn}} \cdot \underbrace{e^{-\alpha_{mn} t}}_{\text{envelope}} \cdot \underbrace{\sin\left(\omega_{\mathrm{r},mn} t\right)}_{\text{sine wave}} \tag{1}$$

with the modal mass [21]

$$M_{mn} = \rho h \int_0^{l_y}\int_0^{l_x} \Theta_{mn}^2 \mathrm{d}x\mathrm{d}y \ , \tag{2}$$

with density ρ, and plate dimensions defined by thickness h, length l_x, and width l_y. Θ_{mn} are the shapes of the individual modes which resonate at angular frequency $\omega_{\mathrm{r},mn}$. All damping is combined in the decay factors α_{mn}. The indices m and n define the mode index (number of nodal lines) in x- and y-direction, respectively. Note that this impulse response describes the vibration of the plate itself and does not account for the radiated or perceived sound.

3.2. Mode shapes and amplitude weights

The 2D mode shapes $\theta_{mn}(x,y) = \theta_m^{\mathsf{T}}(x)\,\theta_n(y)$ are computed numerically as the Cartesian or outer product of the two 1D characteristic beam functions $\theta_m(x)$ in x-direction and $\theta_n(y)$ in y-direction, respectively. Solutions for $\theta_m(x)$ and $\theta_n(y)$ are provided by [22] for all combinations of the three basic boundary conditions: hinged [h], clamped [c], and free [f]. These can be combined in 6 different ways: [hh], [cc], [ff], [cf], [ch], and [fh]. Note that, e.g., [hf] and [fh] are equivalent, and one can be obtained by spatial inversion of the other. The solutions for hinged and clamped boundary conditions are accurate, while those with free edges are only approximate. The mode shapes themselves are independent of width and height of the plate and thus can be pre-computed in normalized coordinates. What changes with geometry, however, is their scaling and thus their corresponding natural frequencies.

As indicated by Eq. 1, the amplitude A_{mn} of a certain mode is obtained by evaluating the respective mode shape $\Theta_{mn}(x_0,y_0)$ at the excitation position. For efficient implementation, the amplitude at the normalized excitation position is returned via bilinear interpolation, which is sufficient for the given amplitude variations.

3.3. Undamped natural frequencies

According to Hamilton's principle [23, p. 964], the motion of an orthotropic plate is governed by four rigidity constants D_i which can be expressed by the more familiar elastic constants Young's modulus E_x in x-direction and E_y in y-direction and in-plane Poisson's ratios ν_{xy} and ν_{yx} [24]. Via an orthotropy factor

$$\Omega = \left(\frac{D_1}{D_3}\right)^{1/4} = \left(\frac{E_x}{E_y}\right)^{1/4} = \left(\frac{\nu_{xy}}{\nu_{yx}}\right)^{1/4} \ , \tag{3}$$

together with isotropic material constants

$$\begin{aligned} E &= \sqrt{E_x E_y} \ , \quad \nu = \sqrt{\nu_{xy}\nu_{yx}} \ , \\ D &= \sqrt{D_1 D_3} = \frac{E}{12(1-\nu^2)} \ , \end{aligned} \tag{4}$$

we formulate them as

$$\begin{aligned} &D_1 = \Omega^2 D \ , \ D_2 = 2\nu D \ , \ D_3 = \frac{1}{\Omega^2} D \ , \\ &\text{and } \ D_4 = G_{xy}/3 \approx \min\left\{\Omega^2, \Omega^{-2}\right\} 2(1-\nu) D \ . \end{aligned} \tag{5}$$

The value of D_4 is based either on the in-plane shear modulus G_{xy} or its rough approximation via data from [25].

In combination with the mode shapes Θ from the previous section and plate dimensions ($l_x \times l_y \times h$), the rigidities D_i describe the maximum potential energy E_{pot} of the plate [22], [24]. On the other hand, the maximum kinetic energy is connected to the modal mass: $E_{\text{kin}} = \omega^2 M_{mn}/2$. After Rayleigh's principle, if the total mechanical energy $E_{\text{pot}} + E_{\text{kin}}$ stays constant, $E_{\text{pot}} = E_{\text{kin}}$ applies for the undamped natural frequencies ω_0, and thus

$$\omega_0^2 = 2E_{\text{pot}}/M_{mn} \ . \tag{6}$$

For the purpose of solving Eq. 6 we define 4 coefficients:

$$\begin{aligned} G_x^4 &= \frac{\iint \left(\frac{\partial^2\Theta}{\partial x^2}\right)^2 \mathrm{d}x\mathrm{d}y}{\Psi} \ , \ H_x H_y = \frac{\iint \frac{\partial^2\Theta}{\partial x^2}\frac{\partial^2\Theta}{\partial y^2}\mathrm{d}x\mathrm{d}y}{\Psi} \ , \\ G_y^4 &= \frac{\iint \left(\frac{\partial^2\Theta}{\partial y^2}\right)^2 \mathrm{d}x\mathrm{d}y}{\Psi} \ , \ J_x J_y = \frac{\iint \left(\frac{\partial^2\Theta}{\partial x\partial y}\right)^2 \mathrm{d}x\mathrm{d}y}{\Psi} \ , \end{aligned} \tag{7}$$

with

$$\Psi = \pi^4 \iint \Theta^2 \mathrm{d}x\mathrm{d}y \ . \tag{8}$$

The undamped natural frequencies $\omega_0 = 2\pi f_0$ then become

$$\omega_0 = \frac{\pi}{\sqrt{48}} \frac{h}{S} c_\mathrm{L} \left[\frac{\Omega^2}{r_\mathrm{a}^2} {G_x}^4 + 2\nu H_x H_y + \frac{r_\mathrm{a}^2}{\Omega^2} {G_y}^4 + \min\{\Omega^2, \Omega^{-2}\} 2(1-\nu) J_x J_y \right]^{1/2} , \tag{9}$$

with surface area $S = l_x \cdot l_y$, aspect ratio $r_\mathrm{a} = l_x / l_y$ (note that $l_x \geq l_y$ and thus $r_\mathrm{a} \geq 1$), and longitudinal wave velocity $c_\mathrm{L} = \sqrt{12D/\rho}$. Analytic solutions to the factors G_x, H_x, and J_x, as well as G_y, H_y, and J_y are provided by [22] for all combinations of the main boundary conditions, analog to the mode shapes in Sec. 3.2. Apart from that, they only depend on the number of nodal lines and can thus be pre-computed.

3.4. Damping

In the impulse response in Eq. 1, the damping is included via the decay factor α_{mn} of the exponential decay of each individual mode. In some cases it is better expressed as loss factor η (sometimes called $\tan\delta$). A constant loss factor leads to a decay factor that rises linearly with frequency f, with slope $\pi\eta$. The loss factor relates to the other parameters via

$$\eta = \frac{1}{Q} = 2\zeta = \frac{2\alpha}{\omega} = \frac{2}{\omega\tau} = \frac{2\ln(1000)}{\omega T_{60}} , \tag{10}$$

with quality factor Q, damping ratio ζ, time constant τ, and $-60\,\mathrm{dB}$ decay time T_{60}. The damping model includes four sources of damping: viscoelastic, thermoelastic, and viscous damping, as well as damping due to ratiation.

Radiation damping. The largest source of damping is the radiation of sound itself. The better a certain mode is radiated, the stronger it is damped. For isotropic plates, the damping due to radiation was formulated by [26] to be

$$\eta_r \approx \mathfrak{Im} \left\{ \frac{2}{\omega_\mathrm{cr}} \frac{\rho_0 c_0}{\rho h} \frac{\sum_{m=1}^{3} b_{\mathrm{r},m} \left(\frac{j\omega}{\omega_\mathrm{cr}}\right)^m}{\sum_{n=0}^{3} a_{\mathrm{r},n} \left(\frac{j\omega}{\omega_\mathrm{cr}}\right)^n} \right\} , \tag{11}$$

with air density $\rho_0 = 1.2\,\mathrm{kg\,m^{-3}}$, sound velocity $c_0 = 344\,\mathrm{m\,s^{-1}}$, as well as the constants $b_\mathrm{r} = [0.0620, 0.5950, 1.0272]$ and $a_\mathrm{r} = [1.1669, 1.6574, 1.5528, 1]$. Above its cutoff frequency, the critical frequency

$$\omega_\mathrm{cr} = \frac{c_0^2}{h}\sqrt{\frac{\rho}{D}} \quad \text{or} \quad f_\mathrm{cr} = \frac{\omega_\mathrm{cr}}{2\pi} , \tag{12}$$

radiation is the predominant source of loss (see Fig. 6). Below, other damping mechanisms are much larger.

Thermoelastic damping appears mainly in metals due to their strong thermal conductivity and thus dissipation of heat created by elastic deformations. According to [26] the thermoelastic loss factors η_t for isotropic plates can be formulated as

$$\eta_{\mathrm{t},mn} \approx \frac{R_\mathrm{1t}}{\frac{h^2\omega}{c_\mathrm{1t}} + \frac{c_\mathrm{1t}}{h^2\omega}} \left(J_{1,mn} + \frac{1}{\nu} J_{2,mn} + J_{3,mn} \right) , \tag{13}$$

with the meta-parameters

$$R_\mathrm{1t} = \frac{8 T_0 \phi^2}{\pi^4 D \rho C} , \quad \phi = \alpha_\mathrm{T} \frac{E}{1-2\nu} , \text{ and } c_\mathrm{1t} = \frac{\kappa\pi^2}{\rho C} , \tag{14}$$

which depend on thermal expansion coefficient α_T, specific heat at constant strain C, thermal conductivity κ, and absolute temperature T_0. Thermoelastic losses additionally depend on the partitioning of potential energy between the four rigidities D_i, which is expressed by the weighting factors

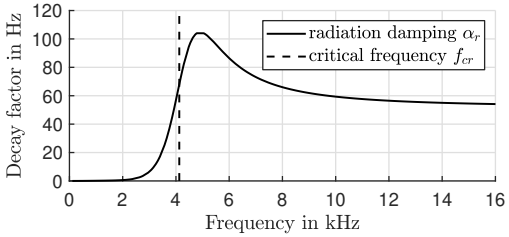

Figure 6: Radiation damping of a 3 mm thick aluminum plate.

$$J_i = \frac{J_i'}{\sum_{i=1}^{4} J_i'} , \tag{15}$$

with (in the isotropic case)

$$J_1' = G_x^4 , \; J_2' = 2\nu H_x H_y , \; J_3' = G_y^4 , \; J_4' = \frac{G_{xy}}{3D} J_x J_y . \tag{16}$$

Due to conservation of energy, $J_1 + J_2 + J_3 + J_4 = 1$ [24].

Viscoelastic damping result from hysteresis due to a combination of viscous and elastic properties and can not be predicted from material constants [27]. For isotropic materials, the viscoelastic loss factor η_v is almost constant over frequency and can thus be approximated by a single value [27]. Average values for common materials are given by Cremer [28, pp. 191, 195–196]. While Chaigne and Lambourg [26] used a physically justified (but more complex) model, their measured loss factors for glass are almost identical to the geometric mean of the range given by Cremer. For wood, the loss factors follow a "standard trend", based on only Young's modulus E and density ρ [29]:

$$\eta_\mathrm{v} = 10^{-1.23} \cdot (E/\rho)^{0.68} . \tag{17}$$

Figure 7 illustrates measured viscoelastic loss factors η_v of several materials as a function of the longitudinal wave velocity c_L. We infer a rough proportionality factor of 57 for wood and plastic, 5.7 for glass, and 0.57 for metal. This simple factor is preferred over a precise fit, as it implies that a traveling wave receives a constant amount of damping per distance traveled, independent of its velocity. As we had the impression that acrylic and wood sounded overly damped, the model is generalized even further to $\eta_{\mathrm{v},\blacksquare} = 5.7/c_\mathrm{L}$ for non-metals and $\eta_{\mathrm{v,M}} = 0.57/c_\mathrm{L}$ for metals.

Viscous damping. In order to account for damping due to external mounting, absorbers, and the viscosity of the surrounding material, we add a constant viscous decay factor α_f, similar to [26]. Values of α_f are given by [26] for aluminum (0.032 Hz), glass (0.88 Hz), carbon (0.8 Hz), and spruce wood (2.4 Hz). We utilize a viscous damping parameter as a simple way to model external interaction such as damping with the palm of the hand. The decay times in the low-frequency range (which otherwise tend to infinity at 0 Hz) are thereby limited, which is common practice in perceptual studies (e.g., [30], [31]).

Complete damping model. According to [31], materials between aluminum and glass can be effectively simulated by blending between thermoelastic and viscoelastic damping with the help of a damping interpolation parameter H. We generalize this approach

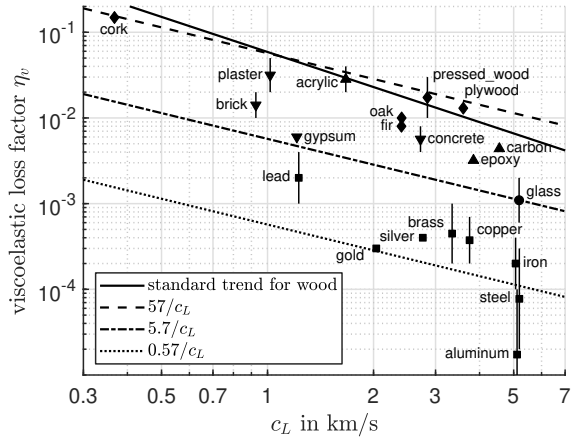

Figure 7: Viscoelastic loss factor η_v as a function of longitudinal wave velocity c_L. Vertical lines represent the range between minimum and maximum value from the literature, while markers represent their geometric mean and gross material category.

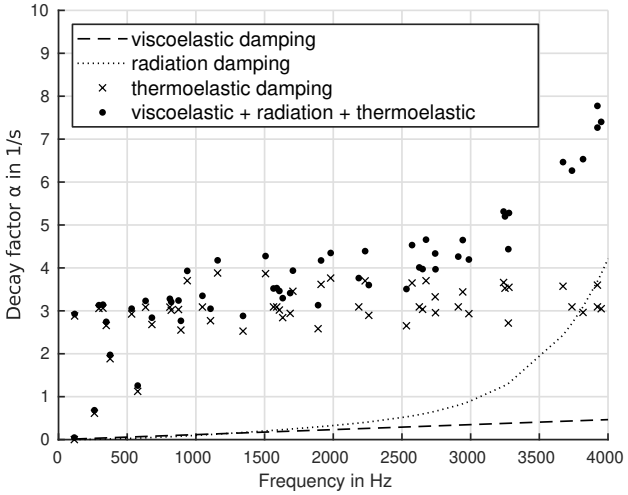

Figure 8: Decay factors α of an aluminum plate due to main damping mechanisms: radiation, thermoelasticity, viscoelasticity.

and interpret H as the metallicity of a material. The overall loss factors of the plate therefore sum up to

$$\eta = (1-H)\eta_{\mathrm{v},\cancel{\mathrm{M}}} + H\left(\eta_{\mathrm{v,M}} + \eta_\mathrm{t}\right) + \eta_\mathrm{r} + 2\alpha_\mathrm{f}/\omega \ . \tag{18}$$

The contribution of the individual damping mechanisms to overall decay factors is depicted in Fig. 8.

3.5. Indentation hardness

Depending on the actual material, a striking mallet usually caves into the plate, leaving an indentation behind. The consequence is a larger area of contact than what elastic deformation (e.g., described by Hertz' law of contact [32]) predicts. The indentation hardness is usually estimated via material probing by a standardized indenter. While there are many standards to choose from, we use the Brinell hardness measure HB, as it applies a spherical indenter and conceptually shares some similarity with a simple excitation model based on Hertz' law of contact. It is usually given in kilogram-force[3] (kgf). Different to other materials, wood is usually specified by Janka hardness F_Janka in N. We convert it to Brinell scale via a rough approximation which is just sufficient for the purpose of sound generation: $HB \approx F_\mathrm{Janka}/(2\pi g R_\mathrm{I}^2) = 0.00051 F_\mathrm{Janka}$, with the usual indenter radius of $R_\mathrm{I} = 5.64\,\mathrm{mm}$.

According to [33], the impact between sphere and plate can be approximated by a force that follows the shape of a Hann- or raised-cosine window over time. In order to avoid a convolution with the window itself, its frequency response is approximated by a 3rd-order low-pass filter, with $-3\,\mathrm{dB}$ cutoff frequency $f_{cH} \approx 0.6555 t_\mathrm{hann}$. From measurements of [32] for xylophone bars struck by mallets of different materials, we can estimate t_hann for rosewood (156 µs) and rubber (625 µs). Based on the measurements by [20], we obtain rough estimates of t_hann for acrylic (160 µs), aluminum (38 µs), and steel (28 µs). A simple linear regression of the resulting cutoff frequencies with respect to the respective Brinell hardness (on a logarithmic scale) already provides a sufficient approximation:

$$\log(f_{cH}) \approx 0.4160 \log(HB) + 7.6783 \tag{19}$$

[3] kilogram-force: a deprecated gravitational metric unit of force; $1\,\mathrm{kgf} = 9.806\,65\,\mathrm{N}$

3.6. Radiation efficiency

For the purpose of auditory augmentation, the simulation of a realistic radiation pattern of the rectangular plate is not necessary. However, the frequency-dependent radiation efficiency is essential for the typical sound. An empirical model for the radiation efficiency of an unbaffled plate, valid for aspect ratios between 1 and 5, was proposed by [21]. They define edge frequencies which depend on physical parameters and divide the radiation efficiency into frequency regions:

$$f_\mathrm{b} = \sqrt{f_1 f_2} \ , \quad f_\mathrm{e} = \frac{c_0}{2\sqrt{S}} \ , \quad \text{and} \quad f_\mathrm{cr} = \frac{1}{2\pi}\frac{c_0^2}{h}\sqrt{\frac{\rho}{D}} \ , \tag{20}$$

with air density ρ_0, sound velocity in air c_0, the surface area of the plate S. f_1 and f_2 are the lowest two natural frequencies of the plate. In case of simply-supported edges, $f_1 = f_{11}$ and $f_2 = f_{21}$. The unlimited radiation efficiency σ' is

$$\sigma' = \sigma_1 = 4S^2 f^4 / c_0^4 \quad \text{for } f \le f_\mathrm{b} \ , \tag{21}$$

$$\sigma' = \sigma_2^\epsilon \, \sigma_1^{1-\epsilon} \quad \text{with} \quad \epsilon = \frac{f - f_\mathrm{b}}{f_2 - f_\mathrm{b}} \quad \text{for } f_\mathrm{b} < f \le f_2 \ , \tag{22}$$

$$\sigma' = \sigma_2 = \sigma_\mathrm{e} \left(f/f_\mathrm{e}\right)^2 \quad \text{for } f_2 < f \le f_\mathrm{e} \ , \tag{23}$$

$$\sigma' = \frac{p c_0}{4\pi^2 S f_\mathrm{cr}} \cdot \frac{\psi}{\left(1-\psi^2\right)^2} + \left(\pi\eta\frac{f}{f_\mathrm{cr}}\right)^{3/2} \quad \text{for } f_\mathrm{e} < f < f_\mathrm{cr} \ , \tag{24}$$

with perimeter $p = 2(l_x + l_y)$ and $\psi = \sqrt{f/f_\mathrm{cr}}$, and

$$\sigma' = \left(1 - f_\mathrm{cr}/f\right)^{-1/2} \quad \text{for } f_\mathrm{e} < f < f_\mathrm{cr} \ . \tag{25}$$

The final radiation efficiency σ is limited to

$$\sigma = \min\left\{\sigma' \, , \quad (0.5 - \frac{0.15}{r_\mathrm{a}})\sqrt{\frac{2\pi f_\mathrm{cr} l_y}{c_0}}\right\} \ . \tag{26}$$

3.7. Subtractive modal synthesis

The physical model itself can be regarded as a parameter conversion which maps from physical parameters to intermediate sound parameters that are then rendered by resonant filters. In particular, we employ a subtractive modal synthesis approach, based on a bank of parallel Smith-Angell resonators [34], [35, pp. 260–261], each with its individual amplitude, frequency, and Q-factor. All resonators are fed with the same input signal; their outputs are summed.

With increasing damping of a certain mode, the effective frequency of the exponentially decaying sinusoid (see Eq. 1) decreases from the ideal ω_0 to a marginally lower one ω_d (Eq. 27). The peak of the resonance appears at the even lower frequency ω_r:

$$\omega_\mathrm{d} = \sqrt{\omega_0^2 - \alpha^2} \ , \quad \omega_\mathrm{r} = \sqrt{\omega_0^2 - 2\alpha^2} \ . \tag{27}$$

Filter frequencies are therefore set so that the peak occurs at ω_r, while both gain and frequency are fine-tuned via the ratio $\omega_0/\omega_\mathrm{d}$. The input gains of the resonators include amplitude weights due to indentation hardness (Sec. 3.5) as well as excitation position and modal mass (Sec. 3.1). The output gains describe the radiation efficiency (Sec. 3.6). Model parameters are set either by external data or by a graphical user interface. Each time a model parameter is changed, the dependent sound parameters are updated and sent to filters in the real-time synthesis engine that runs on the SuperCollider server. An exponential lag of $50\,\mathrm{ms}$ per $60\,\mathrm{dB}$ for all sound parameters ensures smooth transitions.

For some parameters such as boundary conditions, smooth transitions between two states are difficult. In such cases, several *models* are computed and their sound parameters are morphed instead. For cross-fading instead of morphing, both models are rendered by the sound synthesis as individual *layers* whose outputs are mixed. Different spatial *zones* of the interface plate can be defined by arbitrary polygons, each exhibiting one or more layers consisting of one or more models.

4. TECHNICAL CHALLENGES

4.1. Tracking of contact position and hand damping

For realistic and thus plausible auditory augmentation, the location-dependent timbre that is evoked by the mode shapes at excitation postion needs to be taken into account. For that purpose the interacting hand or tool tracked in order to pass the coordinates to the physical model in real time via OSC. Tracking of contact position is achieved in two ways.

Firstly, as a cheap solution, we use a NECO $32\,\mathrm{inch}$ IR multi-touch overlay frame that allows simultaneous tracking of up to 10 individual points $\geq 5\,\mathrm{mm}$ in size. It features an effective tracked region of $702.1\,\mathrm{mm} \times 395.3\,\mathrm{mm}$, and is usually intended to be attached on top of ordinary TV or computer screens. Connected via USB 2, it delivers tracking data in the HID multi-touch protocol[4], including positions as well as sizes of the tracked fingers (or any other objects) as soon as they are located in the tracked space within the frame. A Python script grabs the device (to prevent the operating system from using it), to compute normalized coordinates (between 0 and 1), and to forward these via OSC. The position of the most recently detected point is taken as the current excitation position. For each point, the major and minor axis of an assumed elliptical shape allow a rough estimate of the areas of contact. Their sum is mapped to the viscous damping factor α_f, simulating continuous hand contact. This enables users to dampen the model plate with their hands in a realistic manner.

Highest speed and precision is achieved by infrared tracking, on the cost of reflective markers. Our tracking system consists of 8 OptiTrack Flex 13 cameras with the Motive:Body software on a dedicated PC which streams the real-time tracking data (absolute Cartesian coordinates, orientation quaternion) as OSC through a small wrapper application[5]. Both the tool that mediates the interaction (ball-pen) and the table are tracked through attached markers. The position of the tip of the pen, $\mathbf{p}_\mathrm{tip} = \mathbf{p}_\mathrm{tool} + (\mathbf{R}_\mathrm{tool} \cdot \Delta\mathbf{p}_\mathrm{tool})$, is obtained by the tracked tool position $\mathbf{p}_\mathrm{tool}$, its orientation in form of a rotation matrix[6] $\mathbf{R}_\mathrm{tool}$, and the offset $\Delta\mathbf{p}_\mathrm{tool}$ between tip and tracked tool position in default orientation. It is further transformed by the table to retrieve the excitation position, $\mathbf{p}_\mathrm{ex} = \mathbf{R}_\mathrm{table}^{-1} \cdot (\mathbf{p}_\mathrm{tip} - \mathbf{p}_\mathrm{table}) + \Delta\mathbf{p}_\mathrm{table}$, with position $\mathbf{p}_\mathrm{table}$, offset $\Delta\mathbf{p}_\mathrm{table}$ and rotation $\mathbf{R}_\mathrm{table}$ of the table. x- and y-coordinates are finally normalized (divided by the interface dimensions) and sent to the physical model via OSC. The z-axis (height) is kept in physical units for optional use.

In order to allow damping by the palm of the hand even in case of marker-based tracking, two load cells (range $\leq 5\,\mathrm{kg}$) are placed below the front corners. They connect to an Arduino Pro Micro micro-controller via a pair of HX711 A/D-converters, acting as electronic balance. The Arduino provides a Universal Plug and Play (UPnP) USB MIDI device that forwards both load values as separate control change (CC) messages.[7] The balances are set up and zeroed at startup, automatically adapting to the default load of the interface and possibly placed objects.

4.2. Equalization

In practice, the bending wave loudspeaker that is driven by the exciters does not represent a transparent sound system, but is filtered by the transfer function and radiation pattern of the plate. To overcome such distortions, the outputs require individual calibration. While the same applies to inputs (piezos), their calibration was tested but considered as not necessary in the end. In addition, the impulse responses of the signal path between exciters and piezos are needed for feedback subtraction. Impulse response measurements were carried out by the exponential sine sweep (ESS) method [36]. The test signal was generated in Matlab, based on [37]. The actual measurements were performed in Pd[8] and processed in Matlab. The impulse responses were normalized to the maximum of all channels within each type (exciter to piezo, exciter to microphone) so that the maximum equaled $0\,\mathrm{dBFS}$. The calibration microphones (see block diagram, Fig. 5) were placed at the approximate ear positions of a hypothetical user sitting in front of the apparatus. Their cardioid directivity pattern pointed towards the plate center, to suppress room reflections. The desired equalization filter for a given spectrum is actually its inverse. For real-time application, we seek a causal filter with minimum group delay, i.e., a minimum-phase filter that is based only on the inverted magnitude response, ignoring the phase.

[4] Multi-touch (MT) protocol: e.g., `https://www.kernel.org/doc/html/latest/input/multi-touch-protocol.html`

[5] pyNatNat: `https://git.iem.at/tracking/pyNatNat`

[6] Conversion from quaternion to rotation matrix adopted from the JavaScript 3D library: `https://github.com/mrdoob/three.js`

[7] The source code is provided here: `https://github.com/m---w/HX711_MIDI`

[8] Pure Data (Pd): `https://puredata.info/`

A linear and time-invariant system (or signal path) can be defined by the impulse response $h(t)$ or its spectrum $H(j\omega)$. For better readability, the dependency on $(j\omega)$ is omitted. The measured magnitude spectra $|H_{\mathrm{E}jk}|$ of the exciters $j = \{1, ..., J\}$ are energetically averaged across microphones $k = \{1, ..., K\}$ in order to form $|H_{\mathrm{E}j}|$. The desired equalization filters become

$$H_{\mathrm{out}j} = \mathrm{MP}\left\{\left(|H_{\mathrm{E}j}| + \rho\right)^{-1}\right\} \quad , \tag{28}$$

where ρ is a small regularization parameter and MP is the operation of creating a minimum-phase filter from any given magnitude spectrum. Minimum-phase filters are computed in Matlab:

1. *Low- and high-pass filtering.* Below frequency f_{min} (e.g., 300 Hz for exciters, due to their cutoff frequency) and above frequency f_{max}, the magnitude is set to stay constant. This prevents the filter from boosting frequencies the exciter cannot produce. The result is the desired magnitude spectrum.
2. *Regularization.* A $1/8$-octave smoothing is applied on the magnitude spectrum, to shorten the impulse response and thus reduce computational complexity of the convolution.
3. *Obtain minimum phase.* We seek a stable and causal filter with low group delay and minimum phase: all its poles and zeros must lie within the unit circle. The (real) magnitude spectrum is converted to a (complex) minimum-phase spectrum via the cepstral method, by mirroring the coefficients to the inside of the unit circle. [38, pp. 297–303][9]
4. *IFFT.* Yield the filter impulse response by inverse FFT.
5. *Cropping and Fading.* The impulse response is cropped at its -60 dB decay time. Finally, a fade-out with the shape of a raised cosine (2nd half of a Hann window) is applied to the last 10 % of its duration.

4.3. Noise and feedback control

AltAR/table is a rather unstable feedback system. Not only it implements a closed loop between contact microphones and exciters through the same physical plate, but it even inserts a bank of steep resonant filters within that loop. Without some sort of noise and feedback control, it would blow up before even touching it. To suppress noise from irrelevant frequency regions below 80 Hz and above 10 kHz, the input signal is pre-conditioned by 2nd-order high-pass and low-pass filters, respectively. In addition, a simple noise gate makes sure that the system stays quiet if unused. Feedback is controlled in four different ways that are described below and depicted in Fig. 9.

Keeping in mind the physical sound model, it is obvious that howling will occur at the resonant frequencies themselves. We therefore seek a filter which cancels the effect of the resonator filterbank at the input. We equalize the parallel resonators by a bank of serial notch filters (anti-resonators), so that in consequence, with both filterbanks in series, the magnitude of the resonators are clipped at a settable threshold g_{RT} (see Fig. 10). For the notch filters, we chose constant-Q peaking EQ filters [35, pp. 279–280] set to gains gains $g_{\mathrm{A}mn} = g_{\mathrm{RT}}/g_{\mathrm{R}mn}$, with $g_{\mathrm{R}mn}$ being the combined input and output gains of all gains from Sec. 3 except those connected to excitation position. As the anti-resonator would make the resonator obsolete, a frequency shift is introduced between both filterbanks.

[9] online available: `https://ccrma.stanford.edu/~jos/pasp/Fitting_Filters_Measured_Amplitude.html`

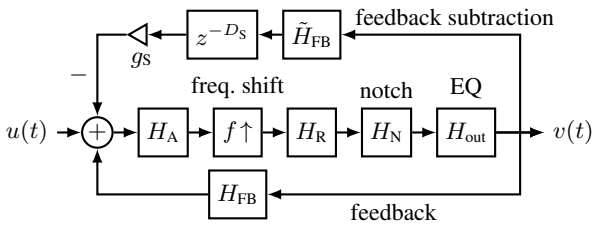

Figure 9: Block diagram of output equalization H_{out} and feedback control, including anti-resonator H_{A}, frequency shift $f\uparrow$, feedback subtraction, and additional notch filters H_{N}.

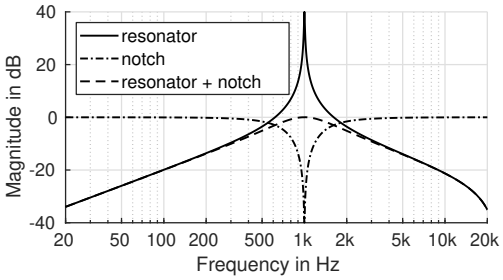

Figure 10: Magnitude responses of a resonator ($f_{\mathrm{r}} = 1$ kHz, $Q = 100$, $g_{\mathrm{R}} = 40$ dB) together with its matched notch EQ (anti-resonator) and the combination of both.

The (parallel) resonators have almost negligible crosstalk, so that their individual peak gains are assumed to remain after summation. In case of high modal density, however, the (serial) notch filters accumulate so that their combined attenuation is overly exaggerated and cannot be simply recovered. We therefore seek corrected optimal gains for a peaking filterbank, i.e., the gains we need to set so that the true peak gains match those of the resonator filterbank. The reciprocal optimal gains are then the command gains of the notch filterbank. The linear equation system (defined by command gains and magnitude responses of the individual filters at all resonant frequencies) can be solved in order to obtain optimal gains for the notch filterbank [39], [40]. In case of identical filter frequencies or high bandwidths, the system matrix might become singular and thus non-invertible, which requires additional regularization. In the lack of a proper linear equation solver in SuperCollider, the command peak gains, peak frequencies, and Q-factors are sent via OSC[10] to a Python script which evaluates the magnitude responses, solves[11] the linear system in a least squares sense and returns the optimal gains. The prior knowledge that the optimal gains lie between zero (no amplification) and command gains (no over-reduction) is set as constraints to the linear solver, which additionally avoids further regularization.

Another strong tool for howling prevention is frequency shifting [41]. Thereby induced inharmonic distortion is acceptable for the broadband impact sounds in our case. We anyway need the frequency shift for moving the signal energy that remains after the anti-resonator into the relevant frequency range of the resonator. The optimal value for the frequency shift is usually half the average frequency distance between two magnitude peaks in the spectrum [42]. For bars and plates, rendered with AltAR/table, we observed

[10] Open Sound Control (OSC): `http://opensoundcontrol.org`

[11] using `lsq_linear` from `scipy.optimize`

an optimal value of 100 Hz — still barely audible for the broadband excitation signal of the impact. The frequency shift is performed via single sideband modulation (SSB), where all frequencies are shifted by a fixed amount, as proposed by [41].[12]

Due to the strong coupling between piezos and exciters, simple feedback suppression is not enough. The feedback path is therefore subtracted from the input signal $u(t)$, in order to reconstruct the true excitation signal $e(t)$ without feedback. The hardware can be assumed to be time-invariant, so that a single measurement of the feedback path impulse responses $h_{\mathrm{FB}ji}$ is sufficient. Note that this is a MIMO (multiple input, multiple output) system which requires J sweeps to obtain the $I \times J$ individual impulse responses (see Sec. 4.2). The impulse responses are cropped at $32\,\mathrm{samples}$ before the shortest signal path delay, as well as after $1024\,\mathrm{samples}$; the first $16\,\mathrm{samples}$ are faded in and the last $10\,\%$ are faded out with a raised-cosine envelope. The global time delay D_{S} and subtraction gain g_{S} are fine-tuned by hand so that $u(t)$ is minimized if pink noise is sent to all outputs at once.

Finally, after activation of the complete system, additional howling frequencies are found by sending pink noise to the outputs and raising the level until howling occurs. As soon as an additional notch filter at the howling frequency is inserted into the signal path, the process is repeated to find more howling frequencies. The system is ready to use if the noise signal can be played back at an adequate level without howling.

5. CONCLUSIONS

With AltAR/table, we now have the technology to create plausible auditory augmentations for any rectangular flat surface. The most obvious use case is the augmented table, but also walls or floors would be conceivable. AltAR/table is more a proof of concept than a final product; for usage as "percussion simulator" in psychoacoustic experiments or in teaching, for sound installations, and for evaluating plausible auditory augmentations for data sonification. It therefore strongly draws on professional audio equipment that may later be replaced by more embedded and miniaturized technology.

The measured total round-trip latency of the running system, including the physical model and all signal processing, equaled $3.7\,\mathrm{ms}$ for the longest signal path (between the piezo and exciter that are farthest apart). This exceptional latency satisfies the recommendations for auditory-tactile environments ($\leq$10 ms) [43] and even for open canal hearing aids ($\leq$5 ms) [44]. A realistic plate with about 100 modes, whose model parameters are changed constantly, leads to high computational effort, mainly due to the equation solver for correcting anti-resonator gains. As audio processing, however, employs only a single processor core, we can afford to load remaining cores with that task.

In upcoming research based on AltAR/table we examine the perception of physical properties of rectangular plates in order to evaluate, how much information can be conveyed through this kind of auditory augmentation.

6. REFERENCES

[1] T. Bovermann, R. Tünnermann, and T. Hermann, "Auditory augmentation", *Int. Journal of Ambient Computing and Intelligence*, vol. 2, no. 2, pp. 27–41, Apr. 2010. DOI: 10.4018/jaci.2010040102.

[2] K. Groß-Vogt, M. Weger, and R. Höldrich, "Exploration of Auditory Augmentation in an Interdisciplinary Prototyping Workshop," St. Pölten, Austria, 2018, pp. 10–16.

[3] M. Weger, T. Hermann, and R. Höldrich, "Plausible Auditory Augmentation of Physical Interaction," in *ICAD*, Houghton, Michigan, 2018, pp. 97–104. DOI: 10.21785/icad2018.024.

[4] R. J. Jacob, A. Girouard, L. M. Hirshfield, *et al.*, "Reality-based interaction: A framework for post-WIMP interfaces", in *CHI*, Florence, Italy: ACM, 2008. DOI: 10.1145/1357054.1357089.

[5] D. Wigdor and D. Wixon, *Brave NUI world: designing natural user interfaces for touch and gesture*. Burlington, Mass: Morgan Kaufmann, 2011, ISBN: 978-0-12-382231-4.

[6] P. Susini, N. Misdariis, G. Lemaitre, *et al.*, "Naturalness influences the perceived usability and pleasantness of an interface's sonic feedback", *Journal on Multimodal User Interfaces*, vol. 5, no. 3, pp. 175–186, May 2012. DOI: 10.1007/s12193-011-0086-0.

[7] R. Tünnermann, J. Hammerschmidt, and T. Hermann, "Blended sonification – sonification for casual information interaction," in *ICAD*, Lodz, Poland, 2013.

[8] T. Hermann and H. Ritter, "Listen to your data: Model-based sonification for data analysis," *Advances in intelligent computing and multimedia systems*, 1999.

[9] T. Stockman, "Listening to people, objects, and interactions", in *ISon*, Stockholm, Sweden, 2010, pp. 3–8.

[10] K. Groß-Vogt, M. Weger, R. Höldrich, *et al.*, "Augmentation of an Institute's Kitchen: An Ambient Auditory Display of Electric Power Consumption," in *ICAD*, Houghton, Michigan, 2018, pp. 105–112. DOI: 10.21785/icad2018.027.

[11] K. Groß-Vogt, M. Weger, M. Frank, *et al.*, "Peripheral Sonification by Means of Virtual Room Acoustics," *CMJ*, vol. 44, no. 1, pp. 71–88, 2021. DOI: 10.1162/comj_a_00553.

[12] R. Tünnermann, S. Zehe, J. Hemminghaus, *et al.*, "Weather to go – a blended sonification application", in *ICAD*, New York, USA, 2014.

[13] M. Iber, P. Lechner, C. Jandl, *et al.*, "Auditory augmented process monitoring for cyber physical production systems", *Personal and Ubiquitous Computing*, Mar. 19, 2020. DOI: 10.1007/s00779-020-01394-3.

[14] J. Hammerschmidt and T. Hermann, "Slowification: An in-vehicle auditory display providing speed guidance through spatial panning," in *ISon*, Bielefeld, Germany, 2016.

[15] J. Hammerschmidt and T. Hermann, "Infodrops: Sonification for enhanced awareness of resource consumption in the shower", in *ICAD*, Lodz, Poland, 2013, pp. 57–64.

[16] S. Bakker, R. van den Berg, S. Pijnappel, *et al.*, "Sounds like home: Sonification and physical interaction in the periphery and center of attention," in *ISon*, 2010, pp. 55–58.

[17] S. Barrass and T. Barrass, "Embedding sonifications in things", in *ICAD*, Łódź, Poland, 2013, pp. 149–152.

[12] for real-time implementations see `FreqShift` in SuperCollider or example `H09.ssb.modulation.pd` in Pd.

[18] A. L. Aldana Blanco, M. Weger, S. Grautoff, *et al.*, "CardioScope: ECG sonification and auditory augmentation of heart sounds to support cardiac diagnostic and monitoring," presented at the ISon, Stockholm, 2019, pp. 115–122.

[19] T. Lossius, P. Baltazar, and T. de la Hogue, "DBAP - distance-based amplitude panning", in *ICMC*, 2011.

[20] P. Troccaz, R. Woodcock, and F. Laville, "Acoustic radiation due to the inelastic impact of a sphere on a rectangular plate", *JASA*, vol. 108, no. 5, pp. 2197–2202, Nov. 2000. DOI: 10.1121/1.1312358.

[21] A. Putra and D. Thompson, "Sound radiation from rectangular baffled and unbaffled plates", *Applied Acoustics*, vol. 71, no. 12, pp. 1113–1125, Dec. 2010. DOI: 10.1016/j.apacoust.2010.06.009.

[22] G. B. Warburton, "The vibration of rectangular plates", *Proceedings of the Institution of Mechanical Engineers*, vol. 168, no. 1, pp. 371–384, Jun. 1954. DOI: 10.1243/PIME_PROC_1954_168_040_02.

[23] T. D. Rossing, Ed., *Springer handbook of acoustics*, 2nd ed., Springer, 2014. DOI: 10.1007/978-1-4939-0755-7.

[24] M. McIntyre and J. Woodhouse, "On measuring the elastic and damping constants of orthotropic sheet materials", *Acta Metallurgica*, vol. 36, no. 6, pp. 1397–1416, Jun. 1988. DOI: 10.1016/0001-6160(88)90209-X.

[25] E. V. Morozov and V. V. Vasiliev, "Determination of the shear modulus of orthotropic materials from off-axis tension tests", *Composite Structures*, 2003.

[26] A. Chaigne and C. Lambourg, "Time-domain simulation of damped impacted plates. i. theory and experiments", *JASA*, vol. 109, no. 4, pp. 1422–1432, Apr. 2001. DOI: 10.1121/1.1354200.

[27] L. Zoghaib and P.-O. Mattei, "Damping analysis of a free aluminum plate", *Journal of Vibration and Control*, vol. 21, no. 11, pp. 2083–2098, Aug. 2015. DOI: 10.1177/1077546313507098.

[28] L. Cremer, M. Heckl, and B. A. T. Petersson, *Structure-borne sound*, 3rd ed. Springer, 2005, ISBN: 978-3-540-22696-3.

[29] T. Ono and M. Norimoto, "Study on young's modulus and internal friction of wood in relation to the evaluation of wood for musical instruments", *Japanese Journal of Applied Physics*, vol. 22, pp. 611–614, Part 1, No. 4 Apr. 20, 1983. DOI: 10.1143/JJAP.22.611.

[30] S. McAdams, A. Chaigne, and V. Roussarie, "The psychomechanics of simulated sound sources: Material properties of impacted bars", *JASA*, vol. 115, no. 3, pp. 1306–1320, Mar. 2004. DOI: 10.1121/1.1645855.

[31] S. McAdams, V. Roussarie, A. Chaigne, *et al.*, "The psychomechanics of simulated sound sources: Material properties of impacted thin plates", *JASA*, vol. 128, no. 3, 2010. DOI: 10.1121/1.3466867.

[32] A. Chaigne and V. Doutaut, "Numerical simulations of xylophones. i. time-domain modeling of the vibrating bars", *JASA*, vol. 101, no. 1, pp. 539–557, Jan. 1997. DOI: 10.1121/1.418117.

[33] S. Schedin, C. Lambourg, and A. Chaigne, "Transient sound fields from impacted plates: Comparison between numerical simulations and experiments", *Journal of Sound and Vibration*, vol. 221, no. 3, pp. 471–490, Apr. 1999. DOI: 10.1006/jsvi.1998.2004.

[34] J. O. Smith and J. B. Angell, "A constant-gain digital resonator tuned by a single coefficient", *CMJ*, pp. 36–40, 1982.

[35] W. C. Pirkle, *Designing Audio Effect Plugins in C++*, 2nd ed. Routledge, 2019, ISBN: 978-0-429-49024-8.

[36] A. Farina, "Simultaneous measurement of impulse response and distortion with a swept-sine technique", in *AES Convention*, Paris, France: Audio Engineering Society, 2000.

[37] K. Vetter and S. di Rosario, "ExpoChirpToolbox: A pure data implementation of ESS impulse response measurement", in *Pure Data Convention*, Weimar, Germany, 2011.

[38] J. O. Smith, *Physical audio signal processing: For virtual musical instruments and audio effects*. W3K, 2010, ISBN: 978-0-9745607-2-4.

[39] J. Abel and D. Berners, "Filter design using second-order peaking and shelving sections", 2004.

[40] V. Välimäki and J. Reiss, "All about audio equalization: Solutions and frontiers", *Applied Sciences*, vol. 6, no. 5, May 6, 2016. DOI: 10.3390/app6050129.

[41] E. Berdahl and D. Harris, "Frequency shifting for acoustic howling suppression", in *DAFx)*, Graz, Austria, 2010.

[42] T. van Waterschoot and M. Moonen, "Fifty years of acoustic feedback control: State of the art and future challenges", *Proc. IEEE*, vol. 99, no. 2, pp. 288–327, Feb. 2011. DOI: 10.1109/JPROC.2010.2090998.

[43] R. H. Jack, A. Mehrabi, T. Stockman, *et al.*, "Action-sound latency and the perceived quality of digital musical instruments: Comparing professional percussionists and amateur musicians", *Music Perception*, vol. 36, no. 1, pp. 109–128, Sep. 2018. DOI: 10.1525/mp.2018.36.1.109.

[44] R. Herbig and R. Chalupper, "Acceptable processing delay in digital hearing aids," *Hearing Review*, vol. 17, no. 1, pp. 28–31, 2010.